Unveiling the Small-scale Jets in the Rapidly Growing Supermassive Black Hole IZw1

The Astrophysical Journal, 966:151 (13pp), 2024 May 10 https://doi.org/10.3847/1538-4357/ad343c

Unveiling the Small-scale Jets in the Rapidly Growing Supermassive Black Hole IZw1

Xiaolong Yang[1,2,3], Su Yao[4,5], Luigi C. Gallo[6], Jun Yang[7], Luis C. Ho[2,8], Minfeng Gu[9], Willem A. Baan[10,11], Jiri Svoboda[12], Ran Wang[2,8], Xiang Liu[10], Xiaoyu Hong[1,3,13], Xue-Bing Wu[2,8], and Wei Zhao[1]
[1] Shanghai Astronomical Observatory, Chinese Academy of Sciences, Shanghai 200030, People's Republic of China; yangxl@shao.ac.cn
[2] Kavli Institute for Astronomy and Astrophysics, Peking University, Beijing 100871, People's Republic of China
[3] Shanghai Key Laboratory of Space Navigation and Positioning Techniques, Shanghai 200030, People's Republic of China
[4] National Astronomical Observatories, Chinese Academy of Science, Beijing 100101, China
[5] Max-Planck-Institut für Radioastronomie, Auf dem Hügel 69, 53121 Bonn, Germany
[6] Department of Astronomy and Physics, Saint Mary's University, Halifax, NS B3H 3C3, Canada
[7] Department of Space, Earth and Environment, Chalmers University of Technology, Onsala Space Observatory, SE-439 92 Onsala, Sweden
[8] Department of Astronomy, School of Physics, Peking University, Beijing 100871, People's Republic of China
[9] Key Laboratory for Research in Galaxies and Cosmology, Shanghai Astronomical Observatory, Chinese Academy of Sciences, 200030 Shanghai, People's Republic of China
[10] Xinjiang Astronomical Observatory, Key Laboratory of Radio Astronomy, Chinese Academy of Sciences, 150 Science 1-Street, 830011 Urumqi, People's Republic of China
[11] Netherlands Institute for Radio Astronomy–ASTRON, NL-7991 PD Dwingeloo, The Netherlands
[12] Astronomical Institute, Academy of Sciences, Boční II 1401, 14131 Prague, Czech Republic
[13] University of Chinese Academy of Sciences, 19A Yuquanlu, Beijing 100049, People's Republic of China
Received 2022 February 26; revised 2024 February 21; accepted 2024 March 13; published 2024 May 2

Abstract

Accretion of black holes at near-Eddington or super-Eddington rates represents the most powerful episode driving black hole growth, potentially occurring across various types of objects. However, the physics governing accretion and jet–disk coupling in such states remains unclear, primarily due to the difficulty in detecting associated jets, which may emit extremely weakly or exhibit episodic behavior. Only a few near/super-Eddington systems have demonstrated radio activity, and it remains uncertain whether jets exist and what their properties are in super-Eddington active galactic nuclei (AGNs) and ultraluminous X-ray sources. This uncertainty stems mainly from the complex radio emission mix, which includes contributions from jets, star formation activity, photoionized gas, accretion disk wind, and coronal activity. In this work, we conducted high-resolution, very long baseline interferometry observations to investigate jets in the highly accreting narrow-line Seyfert I system I Zw 1. Our observations successfully revealed small-scale jets (with a linear size of ∼45 pc) at both 1.5 and 5 GHz, based on the high radio brightness temperature, radio morphology, and spectral index distribution. Additionally, the parsec-scale jet observed in I Zw 1 displays a knotted morphology reminiscent of other sources accreting at similar rates. In summary, the high accretion rates and jet properties observed in the AGN I Zw 1 may support the AGN/X-ray binary analogy in this extreme state.

Unified Astronomy Thesaurus concepts: Active galactic nuclei (16); Accretion (14); Very long baseline interferometry (1769); Radio jets (1347); Seyfert galaxies (1447)

1. Introduction

The Eddington ratio[14] is a key indicator of black hole accretion and ejection states in both stellar-mass black holes (SBHs) and supermassive black holes (SMBHs; e.g., Falcke et al. 2004; Fender et al. 2004; Körding et al. 2006), which is generally <1 under the assumption of spherical accretion. The accretion flows and associated ejection processes with low and moderate Eddington ratios can be generally described with advection-dominated accretion flows (ADAFs; Narayan & Yi 1994; Esin et al. 1997) and standard accretion disk (or Shakura–Sunyaev disk (Shakura & Sunyaev 1973), respectively, and corresponding revisions (e.g., Fender et al. 2004; Done et al. 2007; Yuan & Narayan 2014).

However, supercritical accretion (with the super-Eddington accretion rate for which the black hole radiates above the Eddington luminosity) is viable in both observations and physics and potentially plays an essential role in feeding the growth of the black hole in the early Universe (see Kroupa et al. 2020; Yang et al. 2020, and references therein). Furthermore, super-Eddington accretion of the first-generation SMBHs may have a deep impact on regulating the (host) galaxy evolution and the epoch of reionization through feedback processes. As accretion increases to near or super-Eddington rates, the standard disk geometry cannot be maintained, and the accretion flow will inevitably evolve into a *slim disk* (Vierdayanti et al. 2013). The corresponding state is sometimes called the *ultraluminous state* (Gladstone et al. 2009).

Regardless of the importance and the viability of super-Eddington accretion, our understanding of the accretion and ejection processes in this accretion state remains limited, which is primarily due to that only a few systems can temporarily trigger super-Eddington accretion (e.g., Greiner et al. 2001; Dai et al. 2018), and even fewer systems can maintain long-lived super-Eddington accretion (e.g., Middleton et al. 2021; King et al. 2023). Even worse, the mechanism for sustaining super-Eddington accretion in those sources that persistently accrete at super-Eddington rates is unclear.

It is also widely accepted that SMBHs and SBHs have similarities in accretion physics, i.e., active galactic nuclei (AGNs) and X-ray binaries (XRBs) have similar accretion state

[14] $\lambda_{\rm Edd} \equiv L_{\rm bol}/L_{\rm Edd}$; $L_{\rm bol}$ is the bolometric luminosity, $L_{\rm Edd} = 3.2 \times 10^4\ (M_{\rm BH}/M_\odot) L_\odot$ is the Eddington luminosity, and $M_{\rm BH}$ is the black hole mass.

transitions and associated ejection processes. However, it is still unclear whether the AGN/XRB analogy holds in the ultraluminous state and whether the geometry of the disk corona system and jet-disk coupling are similar. Here, our interest is the connection between the short-lived canonical *very high state* (universally found in XRBs) and the long-standing super-Eddington accretion in, for example, the microquasar SS 433 and ultraluminous X-rays (ULXs), which parameters are driving the long-lived super-Eddington accretion. As the timescale of state transition is proportional to black hole mass (Svoboda et al. 2017; Yang et al. 2020), a very high state in SMBHs (e.g., $M_{\rm BH} = 10^7\,M_\odot$), would last 10^6 times longer than in $10\,M_\odot$ SBHs found in XRBs. Therefore, the study of near/super-Eddington AGNs provides an opportunity to understand the ejection process in a quasi-steady very high state and may shed light on the physics to sustain such a near/super-Eddington accretion. For this reason, we present very long baseline interferometry (VLBI) observations of an AGN, I Zw 1, which radiates close to or above the Eddington limit.

I Zw 1 is one of the closest quasars located at a redshift of $z = 0.0589$ (Ho & Kim 2009) and is regarded as an archetypal narrow-line Seyfert 1 galaxy based on its optical properties (Schmidt & Green 1983; Pogge 2000). The black hole mass of I Zw 1 has been estimated to be $M_{\rm BH} = 9.3 \times 10^6\,M_\odot$ from optical reverberation mapping (Huang et al. 2019). The bolometric luminosity estimated from the spectral fitting is $\log L_{\rm bol} = 45.50$–45.68 erg s^{-1} (Martínez-Paredes et al. 2017), which exceeds its Eddington luminosity with an Eddington ratio of $\lambda_{\rm Edd} = 2.77$–4.20. Another work obtained a higher black hole mass of $M_{\rm BH} = 2.8 \times 10^7\,M_\odot$ using X-ray reverberation (Wilkins et al. 2021) and estimated the Eddington ratio of I Zw 1 as unity (or 0.3) based on the optical monochromatic luminosity (or the X-ray luminosity). However, the authors note that the luminosity could be underestimated due to photons being trapped in the disk. If we take the bolometric luminosity of $\log L_{\rm bol} = 45.50$–45.68 erg s^{-1} (Martínez-Paredes et al. 2017), which is thought to be more accurate than the estimation from the single-band luminosity and use the larger black hole mass measurement of $M_{\rm BH} = 2.8 \times 10^7\,M_\odot$ (Wilkins et al. 2021), then the Eddington ratio would be 0.92–1.40. We should bear in mind that when the bolometric luminosity approaches and exceeds the Eddington luminosity, the actual mass accretion rate would be significantly higher than expected from the observable luminosity assuming a typical radiative efficiency ($\eta < 1$; Bian & Zhao 2003) because of the photon trapping effect (Mineshige et al. 2000). The radiative efficiency of I Zw 1 was estimated, as one of the Palomar–Green (PG) quasars PG 0050+124, to be $\log \eta = -2.21$ or -1.18 ± 0.04 (based on the mass estimates with the broad emission line widths and the M–σ_* correlation, respectively, see Davis & Laor 2011). With such a high Eddington ratio and low radiative efficiency, therefore, the SMBH in I Zw 1 must be growing with a mass accretion rate notably higher than the Eddington limit, i.e., the super-Eddington accretion rate.

I Zw 1 falls into the radio-quiet range with radio-loudness parameter $\mathcal{R} = 0.35$ (fn).[15] (Yang et al. 2020). Radio emission from radio-quiet AGNs is complex and remains a subject of debate (Panessa et al. 2019). On the other hand, the presence of jets in near or super-Eddington systems and how it is launched are also questions that need to be explored. X-ray observations of I Zw 1 indicate that the X-ray corona exhibits some structure, and part of it may be collimated and ejected (Gallo et al. 2007; Wilkins et al. 2017). I Zw 1 is an extreme example of a nearby highly accreting and radio-quiet AGN, providing an ideal laboratory for studying outflow activities,[16] including jets and winds, with high-spatial resolutions.

In this work, we report Very Long Baseline Array (VLBA) and European VLBI Network (EVN) plus enhanced Multi-Element Remote-Linked Interferometer Network (*e*-MERLIN) observations of the nuclear region in I Zw 1, and we also analyze the archival data from VLA and MERLIN. Our paper is organized as follows: Section 2 details the multiband observations, data reduction, and analysis of the target I Zw 1, while Section 3 presents the results and a discussion. Finally, we provide our conclusions in Section 4. Throughout this work, we adopt the standard ΛCDM cosmology with $H_0 = 71$ km s^{-1} Mpc^{-1} and $\Omega_\Lambda = 0.73$, $\Omega_m = 0.27$, and the corresponding physical scale is 1.125 pc mas^{-1} in I Zw 1.

2. Observations and Data Reduction

2.1. VLBI Observation and Data Reduction

We observed I Zw 1 on 2018 September 23, with 10 VLBA antennas, and on 2020 November 17, with 19 EVN antennas plus *e*-MERLIN. The VLBA observation was carried out at the *L* band (1.548 or 1.5 GHz; for short, project code BY145), and the EVN+*e*-MERLIN observation was conducted at the *C* band (4.926 or 5 GHz; for short, project code EY037), respectively. The total VLBA observing time is 2 hr with a data recording rate of 2 Gbps, and the total time of the EVN+*e*-MERLIN observation is 8 hr with a data recording rate of 4 Gbps. Both observations were performed in the phase-referencing mode, using J0056+1341 (R.A.: $00^{\rm h}56^{\rm m}14\overset{\rm s}{.}816010 \pm 0\overset{\rm s}{.}000013$, decl.: $+13°41'15\overset{''}{.}75506 \pm 0\overset{''}{.}00044$) as the phase reference calibrator.

We calibrated the VLBI data in the Astronomical Image Processing System (AIPS), a software package developed by the US National Radio Astronomy Observatory (NRAO; Greisen 2003), following the standard procedure. A prior amplitude calibration was performed using the system temperatures and the antenna gain curves provided by each station. The orientation parameters of Earth were obtained and corrected using the measurements from the US Naval Observatory database, and the ionospheric dispersive delays were corrected based on a map of the total electron content provided by GPS satellite observations.[17] The opacity and parallactic angles were also corrected based on the auxiliary files attached to the data. The delay of the visibility phase and the telescope bandpass were calibrated using the bright radio source 3C 454.3. Next, we performed a global fringe fitting on the phase-referencing calibrator, J0056+1341, by assuming a point source model to solve miscellaneous phase delays.

The phase calibrator J0056+1341 shows a core jet structure that extends up to ∼100 mas to the north (see Figure 7 for their 1.5 and 5 GHz images). We performed self-calibration to the phase calibrator and obtained its CLEAN model, which was then used as the input model to resolve the phases in AIPS. This operation can eliminate phase reference errors due to the jet structure. Finally, both phase and amplitude solutions obtained from the phase calibrator were applied to the target I Zw 1. The

[15] $\mathcal{R} = 1.3 \times 10^5 (L_5/L_{\rm B})$; L_5 is the radio luminosity at 5 GHz and $L_{\rm B}$ is the optical luminosity of the nucleus at $\lambda_{\rm B} = 4400$ Å; radio-quiet AGNs are defined as $\mathcal{R} < 10$.

[16] Throughout the work, we use *outflow* to refer to both collimated jets and wind-like outflows.

[17] https://cddis.nasa.gov

Table 1
Statistical Parameters of Different Image Deconvolution Algorithms

Algorithm	χ_r^2	d.o.f.	σ_r (mJy beam^{-1})	$\sigma_{\rm rms}$ (mJy beam^{-1})	$f_{\rm loss}$
(1)	(2)	(3)	(4)	(5)	(6)
		L band			
Gaussian model fit	1.00524	3,011,564	0.03125	0.02735	0.14
CLEAN	1.00117	3,011,221	0.03012	0.02735	0.10
		C band			
Gaussian model fit	1.000489	1,418,840	0.007362	0.005674	0.29
CLEAN	1.000076	1,418,485	0.007537	0.005672	0.32

Note. Column 1: algorithm for deconvolution; column 2: reduced Chi-squared value; column 3: degrees of freedom; column 4: rms noise in the residual image after subtraction of models; column 5: off-source rms noise in the map; column 6: $\frac{\sigma_r-\sigma_{\rm rms}}{\sigma_{\rm rms}}$ as representative of the unrecovered flux density.

calibrated UV data was exported to DIFMAP (Shepherd 1997) for deconvolution. Based on signal-to-noise ratios (S/Ns) of ∼30 and ∼14 in 1.5 and 5 GHz in the residual map, respectively, we decided not to perform self-calibration on the target source.

We performed different deconvolution algorithms in DIFMAP to produce radio maps, i.e., CLEAN and Gaussian model fit. It is important to note that the solutions for visibilities are not necessarily unique when complex structures are to be handled. To assess the quality of the deconvolution results, we summarized the statistical parameters in Table 1. Obviously, the statistical parameters of the Gaussian model fit are close to CLEAN, while CLEAN is better than the Gaussian model fit based on the χ_r^2value (especially at 5 GHz), which is reasonable as the emission regions are generally more complex than the representation of a few Gaussian components. The resulting CLEAN images and Gaussian model-fitted components are shown in Figure 1. The rms noise in the residual map (column 3 of Table 1) is larger than the off-source rms noise in the map (column 4 of Table 1), indicating that some diffuse emission cannot be recovered in the full resolution map. The off-source rms represent the background noise fluctuation, whereas the rms of the residual map incorporate residual flux densities. Therefore, the loss of flux density in the images can be characterized as $\frac{\sigma_r-\sigma_{\rm rms}}{\sigma_{\rm rms}}$ (column 5 of Table 1). Additionally, we produced a UV-tapered map to reduce the weight of the long-baseline visibilities (and thus also reduce the resolution) in an attempt to recover the weak and extended emission, see panels (a) and (c) in Figure 1.

2.2. Archived VLA Data

We retrieved the raw visibility data of I Zw 1 observed by the Very Large Array (VLA) from the NRAO data archive,[18] including historical VLA and the newly observed Karl G. Jansky VLA (JVLA) data. While some data have been published (see Table 2), to ensure consistency in the data reduction, we performed a manual calibration for all available data sets using the Common Astronomy Software Application (CASA v5.1.1; McMullin et al. 2007). Our data reduction followed the standard routines described in the CASA cookbook. We adopted the flux density standard of Perley & Butler (2017) to set the overall flux density scale for the primary flux calibrator and then bootstrapped the secondary flux density calibrators and the target. For the historical VLA data sets, we determined the gain solutions using a nearby phase calibrator and transferred them to the target I Zw 1. For the JVLA data sets, we also determined antenna delay and bandpass by fringe fitting the visibilities. For the data observed after 1998, we performed an ionosphere correction using the data obtained from the CDDIS archive. Deconvolution, self-calibration, and model fit were performed in DIFMAP. The final images were created using natural weight. Due to the good UV coverage, simple emission structure, and high S/N (S/N > 9), the VLA data allows for self-calibration using a well-established model. For data with a lower S/N, we used three times the image noise as the upper limit for the flux density.

2.3. Astrometry of the VLBI Data

We measure the uncertainties of the astrometric measurements from three main origins: (1) Positional uncertainties of phase-referencing calibrators. In phase-referencing observations, the coordinates of the target are referenced to a close calibrator. The calibrator J0056+1341 was selected from the catalog rfc_2022a in Astrogeo,[19] with precise position with accuracies of $\Delta\alpha = 0.20$ mas in R.A. and $\Delta\delta = 0.44$ mas in decl. and (2) astrometric accuracy of phase-referenced observations, primarily concerning the station coordinate, orientation of Earth, and troposphere parameter uncertainties, which can be measured through the formula and data from Pradel et al. (2006). This portion contributes position errors of $\Delta\alpha \approx 0.26$ mas and $\Delta\delta \approx 0.50$ mas in the VLBA 1.5 GHz observation and $\Delta\alpha \approx 0.27$ mas and $\Delta\delta \approx 0.47$ mas in the EVN+*e*-MERLIN 5 GHz observation, and (3) a thermal error due to the random noise (e.g., Thompson et al. 1986; Rioja et al. 2017). This uncertainty can be characterized as $\sigma_t \sim \theta_{\rm B}/(2 \times {\rm S/N})$, where $\theta_{\rm B}$ is the full width at half-maximum (FWHM) of the restoring beam. In this work, we have taken this value from DIFMAP.

During the self-calibration process, the absolute coordinate position of the phase-referencing calibrator is lost, and the brightest feature of the image is shifted to the phase center of the map. In general, due to the frequency-dependent shift in the peak of the optically thick component and the slightly different distribution of the radio emission at different resolutions, the brightest component may not be the same component from one observation to the next. This induces a systematic offset between two images. The alignment between the images of two frequency

[18] https://archive.nrao.edu/archive/advquery.jsp

[19] http://astrogeo.org/

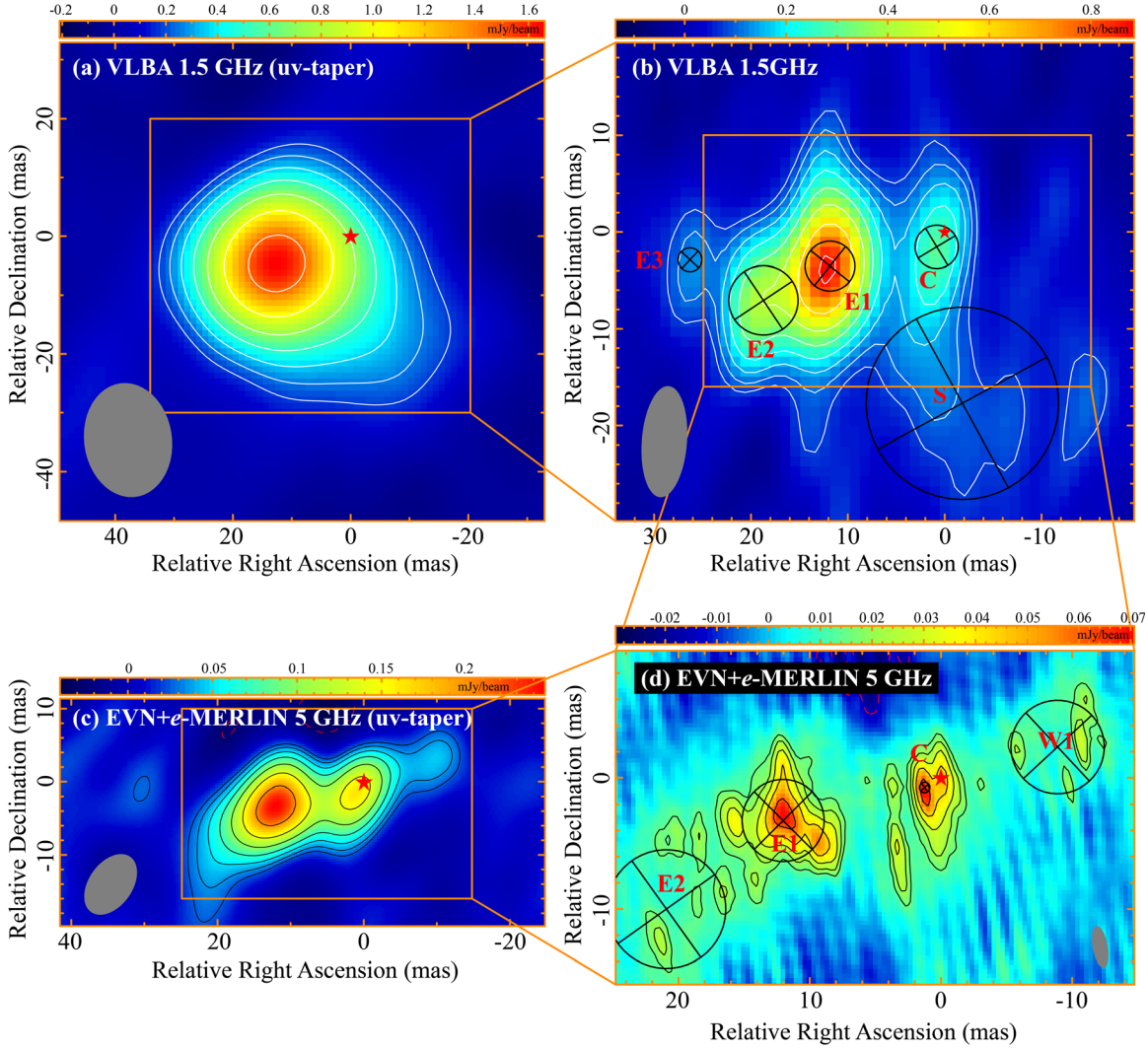

Figure 1. 1.5 and 5 GHz VLBI images of I Zw 1. All the images are produced with natural weight and the map reference is at the position of Gaia. The restoring beams are displayed as gray ellipses in the lower-left/right corner of each panel; their FWHMs and major axis position angles are 19.9 × 14.9 mas at 7.°9, 11.5 × 4.67 mas at −4.°3, 9.27 × 5.95 mas at −35.°1, and 3.22 × 1.14 mas at 10.°1 in panels (a)–(d), respectively. The contours are at $3\sigma \times (-1, 1, 1.41, 2, 2.83,...)$, where positive contours are shown in white (1.5 GHz) and black (5 GHz) solid lines, and negative contours are shown as red hash marks. Panels (a)–(d): the image peak is 1.66, 0.88, 0.24, and 0.10 mJy beam^{-1}, respectively, and the rms noise is 0.06, 0.025, 0.008, and 0.007 mJy beam^{-1}, respectively. The circles with crosses inside indicate the corresponding Gaussian models. In each panel, the red star marks the Gaia optical position. The uncertainty in the position of Gaia is $\Delta\alpha = 0.18$ and $\Delta\delta = 0.17$ mas, which includes an astrometric excess noise error of 0.14 mas. At the redshift of I Zw 1, 1 mas corresponds to 1.125 pc.

observations can be done using an optically thin component as a reference since its position is less affected by the frequency-dependent opacity effect (e.g., Marr et al. 2001; Kovalev et al. 2008; Sokolovsky et al. 2011; Fromm et al. 2013).

In our VLBI observations, we used J0056+1341 as the phase-referencing calibrator, which has a flat-spectrum radio core. We obtained VLBI C (4.34 GHz) and *X*-band (7.62 GHz) data from Astrogeo. As neither the *C*- and *X*-band data are self-calibrated, the core shift at the *C* band can be directly estimated as ΔR.A. ∼0.69 mas, Δdecl. ∼ −0.29 mas relative to the *X*-band data (see Table 3). J0056+1341 also has a significant offset between the *C* and *L* bands (see Figure 7) in our observations, and the offset of the VLBA *L*-band image is determined using the optically thin component J1 of the jet, estimated as ΔR.A. =1.742 mas and Δdecl. = −3.228 mas (see Table 3) relative to the EVN+*e*-MERLIN *C*-band image.

For the target I Zw 1, we use the position of the brightest optically thin ($\alpha = -0.86 \pm 0.07$) component in the tapered EVN+*e*-MERLIN 5 GHz image (panel (c) of Figure 1) to align with the VLBA 1.5 GHz image. The peak position of the 1.5 GHz image was moved in DIFMAP to align with the 5 GHz image by ΔR.A. = 1.33 ± 0.38 mas and Δdecl. = -0.77 ± 0.69 mas, where the positional uncertainties account for both 1.5 and 5 GHz astrometric uncertainties of the brightest component E1. The centroid of the optical emission obtained from the second data release[20] of the Gaia mission (Gaia Collaboration et al. 2018a, 2018b) is R.A. = $00^{h}53^{m}34^{s}.933288 \pm 0.000012$ and decl. = $+12°41'35''.93081 \pm 0.00017$ (J2000). This includes an astrometric excess noise error of 0.14 mas. The coordinates for the target are also listed in Table 3.

2.4. Radio Spectrum

To obtain the radio spectral index α (fn.[21]), we first checked the variability of I Zw 1. Figure 2 shows the radio flux density

[20] https://gea.esac.esa.int/archive/

[21] $S_\nu \propto \nu^{\alpha}$; S_ν is the flux density and ν is the frequency.

Table 2
Summary of Historical Observations and Results for I Zw 1

Telescope	ν (GHz)	Obs. ID	Reference	Date	TOS (min)	BW (MHz)	θ_{maj} (arcsec)	θ_{min} (arcsec)	P.A. (deg)	S_i (mJy)	S_p (mJy beam^{-1})
VLA D	1.49	AE0022	(1)	1983-07-04	2.7	100	52.7	44.8	−14.9	8.40 ± 1.40	8.40 ± 1.17
VLA D	1.40	NVSS*	(2)	1993-11-15	0.4	50	46	46	0	8.80 ± 1.00	7.60 ± 0.46
VLA D	1.40	AV0226	…	1996-09-17	238	6.2	59.2	53.4	25.0	8.43 ± 0.31	8.37 ± 0.30
VLA D	1.40	AV0226	…	1996-09-28	237.5	6.2	59.6	53.5	22.5	8.25 ± 0.32	8.27 ± 0.30
VLA C	1.49	AB0417	(3)	1986-11-08	9.5	100	18.9	14.9	−35.1	6.68 ± 0.67	6.12 ± 0.57
VLA C	1.34	AL0417	…	1997-07-18	190.8	12.5	10.2	8.83	5.19	6.45 ± 0.48	6.51 ± 0.39
VLA C	1.34	AL0417	…	1997-07-24	195	12.5	11.1	8.34	−33.2	6.49 ± 0.41	6.17 ± 0.40
VLA B	1.49	AG0173	…	1985-04-22	85	100	5.94	4.69	52.4	5.13 ± 0.73	4.19 ± 0.43
VLA B	1.40	FIRST	(4)	2011-03-26	1	256	4.3	4.3	0	5.30 ± 0.24	5.05 ± 0.15
VLA A	1.42	AL0502	…	1999-08-26	5.5	100	1.36	1.27	10.9	5.18 ± 0.27	6.77 ± 0.24
VLA A	1.42	AK0406	…	1995-07-20	6.1	100	1.68	1.41	−0.62	5.17 ± 0.19	4.89 ± 0.16
VLA A	1.42	AC0624	…	2002-05-02	10.5	100	1.66	1.36	−5.28	5.28 ± 0.16	4.90 ± 0.13
Arecibo	2.38	*	(5)	1975-08-01		16	162	162	0	4.00 ± 4.00	
VLA BnA	2.98	VLASS1.1*	(6)	2017-10-08	0.1	2048	3.06	2.28	52.7	3.71 ± 0.33	2.87 ± 0.11
VLA BnA	2.98	VLASS2.1*	(6)	2020-07-16	0.1	2048	2.68	2.37	36.6	3.63 ± 0.35	2.72 ± 0.17
VLA D	4.86	AE0022	…	1983-07-04	12.7	100	12.9	11.1	−10.5	3.16 ± 0.18	2.27 ± 0.10
VLA C	4.86	AK0298	…	1992-05-18	27.5	100	9.83	4.90	55.9	2.80 ± 0.11	1.33 ± 0.04
VLA C	4.86	AB0417	(3)	1986-11-08	9	100	5.56	4.72	−33.9	2.46 ± 0.15	2.47 ± 0.08
VLA B	4.86	AL0454	…	1998-09-02	8.6	100	1.51	1.38	7.61	2.20 ± 0.09	2.13 ± 0.05
VLA A	4.86	AK0096	(7)	1983-11-24	25.1	100	0.50	0.42	−29.1	1.84 ± 0.08	1.79 ± 0.04
VLA A	4.86	AK0406	…	1995-07-20	9.5	100	0.49	0.41	−2.14	2.18 ± 0.06	2.02 ± 0.05
VLA A	4.86	AC0624	…	2002-05-02	9.8	100	0.48	0.41	11.6	1.84 ± 0.09	1.85 ± 0.05
MERLIN	4.99	96DECA	…	1996-12-14	558	15	0.08	0.05	22.35	1.46 ± 0.22	1.43 ± 0.11
MERLIN	4.99	97NOVC	…	1997-11-06	450	15	0.08	0.04	20.04	1.51 ± 0.52	1.83 ± 0.27
VLA B	8.46	AC0624	…	2002-08-09	9.8	100	0.68	0.65	20.2	1.46 ± 0.07	1.15 ± 0.03
VLA A	8.44	AP0212	…	1991-06-25	14.8	100	0.26	0.24	59.7	0.94 ± 0.10	0.90 ± 0.05
VLA A	8.44	AB0670	…	1992-12-04	119.3	100	0.27	0.26	−12.2	1.18 ± 0.03	1.09 ± 0.01
VLA C	14.94	AA0048	(3)	1985-07-28	14.5	100	1.87	1.49	−29.5	1.20 ± 0.46	1.20 ± 0.26
OVRO 40	20.00	*	(1)	1983-07-07		400	90	90	0	<1.90	<1.90
VLA C	22.46	AA0048	(3)	1985-07-28	29	100	1.13	1.01	−48.9	<1.91	<1.91
VLA A	22.46	AP0210	…	1991-07-02	18.5	100	0.38	0.09	−56.8	<1.76	<1.76
ALMA	108.64	*	(8)	2016-08-01	4.0		0.57	0.46		0.49 ± 0.07	

Notes. Column 1: telescope; column 2: frequency; column 3: project ID and references for data sets publication (* denotes that original data is not available and that the result is from the literature); column 4: observing date; column 5: time on-source; column 6: observing bandwidth; columns 7–9: beam major axis, minor axis, and position angle; column 10: integrated flux density; column 11: peak flux density.
References: (1) Edelson (1987), (2) Condon et al. (1998), (3) Barvainis & Antonucci (1989); Barvainis et al. (1996), (4) White et al. (1997), (5) Dressel & Condon (1978), (6) Lacy et al. (2020), (7) Kellermann et al. (1989), (8) Tan et al. (2019).

versus the observing epoch. The largest variability we identify is ∼8%, which is from the VLA A-array observations at the *C* band between epochs 1983 and 1995. Since there is no evidence for extreme variability on a timescale of ∼30 yr, we plot the radio flux density versus the frequency in Figure 3 using all archival data. The least-squares fitting gives an overall radio spectral index of -0.89 ± 0.10. From Figure 3, we can see that the radio flux density changes with the characteristic size of the emission regions. The radio spectral index between 1.4 and 5 GHz, using the data sets obtained from similar beams (FWHM sizes; i.e., 1.″3–1.″5 and 4.″3–5.″3), is -0.69 ± 0.08 and -0.61 ± 0.02, respectively. These yield flatter spectral indices than the overall fit. Given the total flux density in Section 2.5, the spectral index between VLBA 1.5 and EVN+*e*-MERLIN 5 GHz is -1.06 ± 0.13, consistent with the overall radio spectral index.

To obtain the spectral index distribution for the high-resolution data observed with the VLBA and EVN+*e*-MERLIN, we created a spectral index map following the procedure described in Hovatta et al. (2014). Here, we used the UV-tapered image by 0.5 at 20 Mλ at 5 GHz and restored it to match the 1.5 GHz map. Similarly, the alignment of two images is through the brightest optically thin component E1. The spectral index was calculated pixel by pixel between the 1.5 and 5 GHz total intensity maps. For a given frequency, pixels with an intensity less than $3\sigma_{rms}$ were removed. The spectral index map between 1.5 and 5 GHz is shown in the left panel of Figure 4. Both the position of Gaia and component C are in the least-steep spectral region ($\alpha > -0.5$; see also Figure 5.)

We study the radio spectral index distribution along the jet trajectory by estimating the ridge line of the jet. We define the jet ridge as the line that connects the peaks of one-dimensional Gaussian profiles fitted to the profile (slices) of the jet brightness drawn orthogonally to the jet direction (see Vega-García et al. 2020). To obtain the ridge line, we performed a fitting to the tapered and restored (with circular beam) 5 GHz EVN+*e*-MERLIN image. The first slice starts from the position of Gaia, and a position angle of 220° (the east direction anticlockwise) was initially adopted for the jet direction. The step

Table 3
Coordinates of the Calibrator J0056+1341 and the Target I Zw 1

Observed Feature	α (J2000) (hh:mm:ss.s)	$\Delta\alpha$ (s)	δ (J2000) (° ′ ″)	$\Delta\delta$ (″)
(1)	(2)	(3)	(4)	(5)
J0056+1341				
J1 at 1.5 GHz	00:56:14.816082	0.000002	+13:41:15.76430	0.00014
J1 at 5 GHz	00:56:14.8159647	0.0000008	+13:41:15.767536	0.000039
The brightest feature at 4.34 GHz (Astrogeo)	00:56:14.8161000	0.0000002	+13:41:15.754988	0.000009
The brightest feature at 7.62 GHz (Astrogeo)	00:56:14.8160522	0.0000001	+13:41:15.755279	0.000005
I Zw 1				
Gaia DR2	00:53:34.933288	0.000012	+12:41:35.9308	0.00017
The brightest feature at VLBA 1.5 GHz (E1)	00:53:34.934176	0.000015	+12:41:35.9267	0.00022
The brightest feature at EVN 5 GHz (E1)	00:53:34.934112	0.000012	+12:41:35.9275	0.00017

Note. The position errors presented here are only from random noise.

Table 4
Model-fitting Results of the Radio Components Detected in I Zw 1 with the VLBA 1.5 GHz and EVN+*e*-MERLIN 5 GHz Observations

Component	ν (GHz)	R.A. Off (mas, J2000)	Decl. Off (mas, J2000)	S_i (mJy)	Size (mas)	$\theta_{\rm lim,maj} \times \theta_{\rm lim,min}$ (mas)	$\log T_{\rm B}$ (K)
(1)	(2)	(3)	(4)	(5)	(6)	(7)	(8)
C	1.548	$>0.55 \pm 0.38$	-1.31 ± 0.76	0.42 ± 0.05	4.5	1.60×0.64	7.22
E1	1.548	11.67 ± 0.26	-3.31 ± 0.50	1.28 ± 0.08	5.1	0.92×0.36	7.57
E2	1.548	18.60 ± 0.52	-6.88 ± 0.66	0.73 ± 0.07	7.2	1.21×0.48	7.05
S	1.548	-2.12 ± 1.51	-17.61 ± 2.24	0.74 ± 0.10	20.0	3.06×1.22	6.17
E3	1.548	26.25 ± 0.71	-2.65 ± 1.56	0.12 ± 0.05	2.4	1.20×0.48	7.19
C	4.926	1.26 ± 0.21	-0.77 ± 0.46	0.15 ± 0.01	0.7	0.62×0.22	7.29
E1	4.926	12.05 ± 0.27	-3.29 ± 0.47	0.47 ± 0.05	6.2	0.54×0.19	5.97
E2	4.926	20.95 ± 0.98	-10.04 ± 1.00	0.15 ± 0.03	9.0	0.31×0.11	5.17
W1	4.926	-8.85 ± 0.68	2.31 ± 0.82	0.11 ± 0.02	7.1	0.86×0.30	5.26

Note. Column 1: component name; column 2: frequency; columns 3 and 4: R.A. and decl. offset corresponding to the Gaia DR2 position; column 5: integrated flux density; column 6: the angular size of components from a Gaussian model fit; column 7: resolution limit along the direction of the major and minor axes of the synthesized beam; column 8: lower limit of the radio brightness temperature.

between individual slices was set to be smaller than the beam size (a measure taken in order to ensure the continuity of the brightness profiles recovered from adjacent slices). The jet direction was readjusted among every three ridge line points. The resulting jet ridge line and spectral index distribution are presented in Figure 4.

2.5. Radio Flux Density and Brightness Temperature

We estimate flux density uncertainties following the instructions described by Fomalont (1999). In this work, the integrated flux densities S_i were extracted from the Gaussian model fit in DIFMAP, where a standard deviation in model fit was estimated for each component and considered as the fitting noise error. Additionally, we assign the standard 5% and 10% errors originating from amplitude calibration of VLBA (see VLBA Observational Status Summary 2018B[22]) and EVN (e.g., Radcliffe et al. 2018) data, respectively.

The radio brightness temperature was estimated using the formula (Ulvestad et al. 2005)

$$T_{\rm B} = 1.8 \times 10^9 (1+z) \frac{S_i}{\nu^2 \phi_{\rm min}\, \phi_{\rm maj}}\ ({\rm K}), \qquad (1)$$

where S_i is the integrated flux density of each Gaussian model component in units of millijansky (column 5 of Table 4), $\phi_{\rm min}$ and $\phi_{\rm maj}$ are the minor and major axes of the Gaussian model (i.e., FWHM) or the restored beam in milliarcsec, ν is the observing frequency in gigahertz (column 2 of Table 4), and z is the redshift.

The resolution limit $\theta_{\rm lim}$ for Gaussian components can be estimated using the formula (Lobanov 2005)

$$\theta_{\rm lim} = 2^{2-\beta/2}\theta_{\rm B}\left(\frac{\ln(2)}{\pi}\ln\frac{\rm S/N}{\rm S/N-1}\right)^{1/2}, \qquad (2)$$

where $\theta_{\rm B}$ is the FWHM of the synthesized beam and $\beta = 2$ is the natural weight. If the fitted component size is lower than the corresponding resolution limit, then $\theta_{\rm lim}$ was used instead as the component size, and the component was identified as unresolved (or the radio-emitting region cannot be constrained). The resolution limits for each component are listed in column 7 of Table 4, and the estimated 1.5 and 5 GHz radio brightness temperatures are listed in column 8. Since the measured component size is only the upper limit, the radio brightness temperature should be considered as the lower limit. We also estimated a total radio flux density from a UV-tapered

[22] https://science.nrao.edu/facilities/vlba/docs/manuals/oss2018B

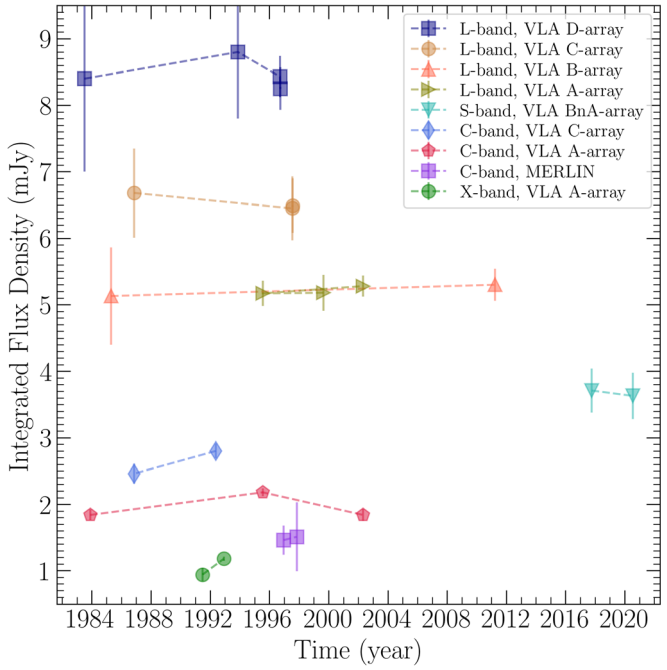

Figure 2. The radio light curves of I Zw 1 over a time interval of 37 yr. The integrated radio flux densities and their uncertainties are taken from Table 2, where the data with the same observing band (approximately equal central frequencies) and arrays/subarrays are concatenated to show the variability.

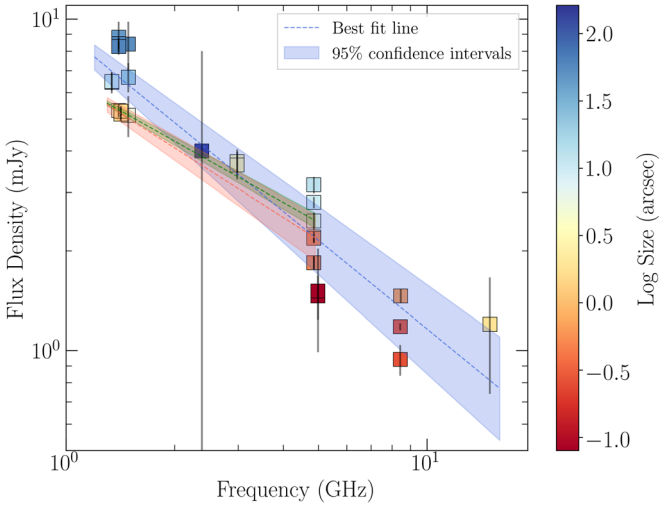

Figure 3. Wide-band radio spectrum of I Zw 1. The integrated radio flux density measurements of I Zw 1 in five radio frequency bands between 1.4 and 15 GHz are shown, where the flux density and uncertainties are taken from Table 2. The blue-dashed line denotes the model-fitting result with a power-law spectrum using all the data points presented here. The power-law slope (spectral index) is −0.89, and the blue belt shows a 95% confidence interval (0.10). The green- and red-dashed lines show the power-law fitting between the 1.4 and 5 GHz data sets with similar size scales, i.e., $1\overset{''}{.}3$–$1\overset{''}{.}5$ (red) and $4\overset{''}{.}3$–$5\overset{''}{.}3$ (green), respectively. The green and red belts indicate their 95% confidence intervals.

image, which is 2.636 ± 0.282 and 0.765 ± 0.085 mJy for 1.5 and 5 GHz, respectively, and the corresponding source angular sizes are ∼50 and ∼40 mas, respectively.

3. Results and Discussion

3.1. A Canonical Jet in the Super-Eddington AGN I Zw 1.

Panel (b) of Figure 1 shows the 1.5 GHz VLBA image, displaying a quasicontinuous emission structure elongated along the east–west direction with an extent of ∼45 pc. Panel (d) of Figure 1 shows a higher-resolution (the beam FWHM is 3.22×1.14 mas) image obtained from the 5 GHz EVN+*e*-MERLIN observation. The bright components in the 1.5 GHz image are resolved into a series of knots in the 5 GHz image. Most of these components (except for components S and W1) have brightness temperatures $>10^7$ K (Table 4), and the whole radio-emitting structure has an overall steep spectrum (Figure 3), which favors a jet origin and is unlikely from star-forming activities (Condon et al. 1991) and thermal free–free radiation of the hot molecular disk surrounding AGNs (Gallimore et al. 1997). Furthermore, based on the identification of optical and radio cores (see below), the bilateral radio structures in the 5 GHz EVN image (panel (d) of Figure 1) are consistent with the assembling of approaching and receding jets.

The asymmetry in brightness observed between the two branches of the bilateral structures may arise from several factors. These include intrinsic differences in the jets (Fendt & Sheikhnezami 2013), as well as variations in the surrounding ambient medium, notably the effects of the obscuring torus, as explored by studies (e.g, Kameno et al. 2003; Kadler et al. 2004; Fromm et al. 2018; Baczko et al. 2019). Additionally, the Doppler boosting effect, as highlighted in recent work by Janssen et al. (2021), could also play a role, either independently or in combination with other factors. Interestingly, the absence of a prominent radio core in VLBI images of I Zw 1 could be attributed to free–free absorption by the torus, a hypothesis supported by findings from studies (e.g., Vermeulen et al. 2003; Kadler et al. 2004; Fromm et al. 2018; Baczko et al. 2019). Examining the Doppler boosting effect further, we can analyze the ratio of brightness temperatures between the jet and counter-jet components. By using components E1 and W1 at the *C* band, situated at similar distances from the central engine, we find this ratio to be 1.135. Given the radio spectral index of −1 and the estimated inclination angle ranging from 33°–51° (Schinnerer et al. 1998; Costantini et al. 2007), this requires jet velocities between $0.025c$ and $0.034c$ (Urry & Padovani 1995; Kadler et al. 2004) to satisfy a Doppler boosting origin. However, no significant variabilities in radio flux density disfavor the strong Doppler boosting effect. Further investigations through kinematic measurements and flux density variability observations are warranted to elucidate the contribution of the Doppler boosting effect to the observed jet asymmetry.

3.2. Formation of the Clumpy Jet Structures

The jet base of an AGN typically has a flat radio spectrum, due to the synchrotron self-absorption in the optically thick region ($\alpha > -0.5$). The radio core of I Zw 1 is likely close to component C because it is located in the least-steep spectral region (see Figure 4), has a high radio brightness temperature of $\log(T_B/\mathrm{K}) > 7$ at both 1.5 and 5 GHz (see Table 4), and is roughly associated with the position of Gaia. The 5 GHz image further resolves component C and measures a more accurate position of its peak, which is slightly offset from the position of Gaia (see panel (d) of Figures 1 and 5). It has already been shown that there is a significant offset between the VLBI and the positions of Gaia in AGNs (Kovalev et al. 2017; Petrov & Kovalev 2017; Plavin et al. 2019). Interestingly, the offset

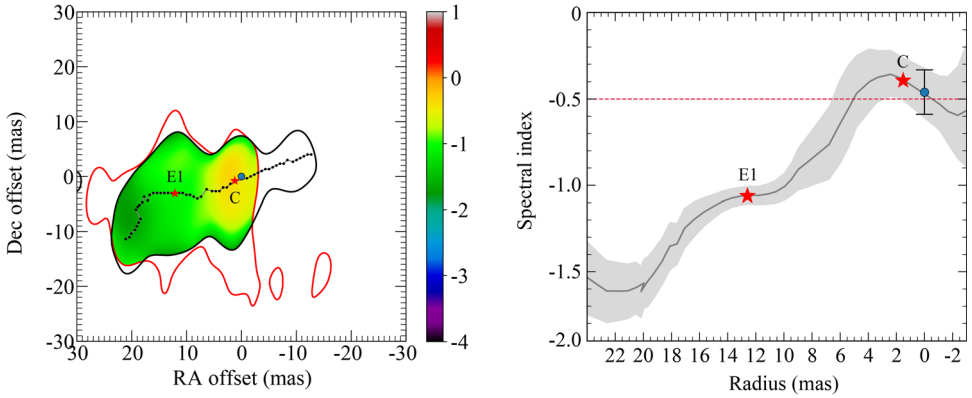

Figure 4. 1.5–5 GHz spectral index distribution of I Zw 1 on the parsec scale. Left panel: the spectral index map produced by using the naturally weighted clean map at 1.5 and 5 GHz. The region with radio flux density below 3σ was set as blank (white), i.e., the outer region of the red (1.5 GHz) and black (5 GHz) curves. Radio spectral indices within both red and black curves are reliable. The black dots and the gray line indicate the ridge line obtained from the tapered 5 GHz EVN+*e*-MERLIN image. The red stars indicate the centroid positions of the Gaussian components E1 and C from the 5 GHz image. Right panel: the spectral index distribution along the ridge line. A positive radius corresponds to positive R.A. coordinates, and vice versa. The position of Gaia is set as the reference. The gray belt marks the uncertainty of the spectral indexes along the ridge line. The red stars mark the locations of the Gaussian components E1 and C from the 5 GHz image. In both panels, the blue asterisks indicate the position of Gaia.

between component C and the position of Gaia is consistent with the observations of Seyfert I galaxies (i.e., the upstream offsets of the positions of Gaia correspond to the VLBI positions, see Plavin et al. 2019). Therefore, the VLBI/Gaia offset in I Zw 1 can be attributed to the dominance of the accretion disk in the optical band (the position of Gaia), while the VLBI observations alternatively track the emissions of jets (Plavin et al. 2019).

Based on both the radio and optical cores, there is an obvious spectral steepening along the eastern jets, while it is less prominent in the western jet (see the right panel of Figure 4). This property resembles canonical jets in blazars and can be explained by the radiative losses of the synchrotron-emitting plasma or with the evolution of the high-energy cutoff in the electron spectrum (Hovatta et al. 2014).

3.3. Formation of the Clumpy Jet Structures

Component C is most likely the closest component to the nucleus; however, the spectrum of C itself is too steep (as a reference, the spectral index at the peak position of component C is roughly -0.4 in the spectral index map, see Figure 5) to be the radio core of I Zw 1. Taking the integrated flux density of C at 1.5 and 5 GHz (see Table 4), we can estimate the 1.5–5 GHz spectral index of component C as -0.88 ± 0.11. Recalling the offset between the VLBI position of component C and the position of Gaia of the optical nucleus, the least-steep spectral region can be attributed to an absorption feature, while it is more probable that component C represents a knot near the nucleus of the jet.

Interestingly, the positions of local brightness enhancements (the knots E1 and W1) are symmetric (see Figure 6), and components E1 and C seem to be embedded on a continuous background of the jet stream and mimic discrete blobs/knots. On the origin of the knots, several works envisage them as the shocks traveling along the jets (e.g., Hovatta et al. 2014), while other works have interpreted them as discrete blobs from episodic ejection (e.g., Shende et al. 2019). We note that the relatively flatter spectra around the Gaussian components (C and E1) in Figure 4 do imply the shock acceleration in the discrete blobs (C and E1) in I Zw 1 (see Hovatta et al. 2014). However, it seems that the heavily knotted jets (compared with the jets in blazars; Hovatta et al. 2014) in I Zw 1 is inconsistent with the only mild flattening in the spectrum, i.e., the spectral distribution shows only plateaux rather than clear bumps (see Hovatta et al. 2014). Alternatively, two additional scenarios can explain this symmetrical positioning and knotted morphology of the jet. First, the presence of quasicontinuous and precessing jets may form a helical jet structure, leading to changes in the viewing angle and consequently affecting the flux density. Second, jet ejection occurs episodically.

Several mechanisms can contribute to the formation of a helical jet structure. If the axis of the accretion disk is tilted relative to the spin of the black hole, the frame-dragging effect generated by the rotating black hole can cause particles within the disk to precess (known as the Lense–Thirring effect (Lense & Thirring 1918)). This effect diminishes with distance from the black hole, becoming insignificant at large distances. Consequently, an inclined viscous accretion disk with respect to the spin of the black hole will produce warps in the disk, which force the alignment between the axis of the innermost accretion disk and the spin of the black hole, a phenomenon termed the Bardeen–Petterson effect (Bardeen & Petterson 1975). The direction of the jet serves as a valuable indicator of the black hole's spin (Blandford & Znajek 1977) and the orientation of the inner accretion disk (Blandford & Payne 1982), with the jet aligning either along the black hole's spin direction or the axis of the inner accretion disk. Our observations of I Zw 1 reveal that the jet direction closely aligns with the kiloparsec-scale molecular disk (Tan et al. 2019; Shangguan et al. 2020), suggesting that the orientation of the kiloparsec-scale molecular disk (axis direction) may be tilted with respect to the axis of the inner accretion disk or the black hole's spin, hinting at the long-term evolution of the accretion disk. The period of Lense–Thirring precession, in minutes, is given by $P \propto M/a_*$, where M is the black hole mass in solar masses, and a_* is the dimensionless black hole spin parameter. Recent X-ray measurements estimated the spin parameter of I Zw 1 to be >0.9 (Wilkins et al. 2021), resulting in precession periods ranging from 20–60 yr in I Zw 1. The identification of jet precession in I Zw 1 will provide insights confirming that precession is likely a common property of accretion at near/

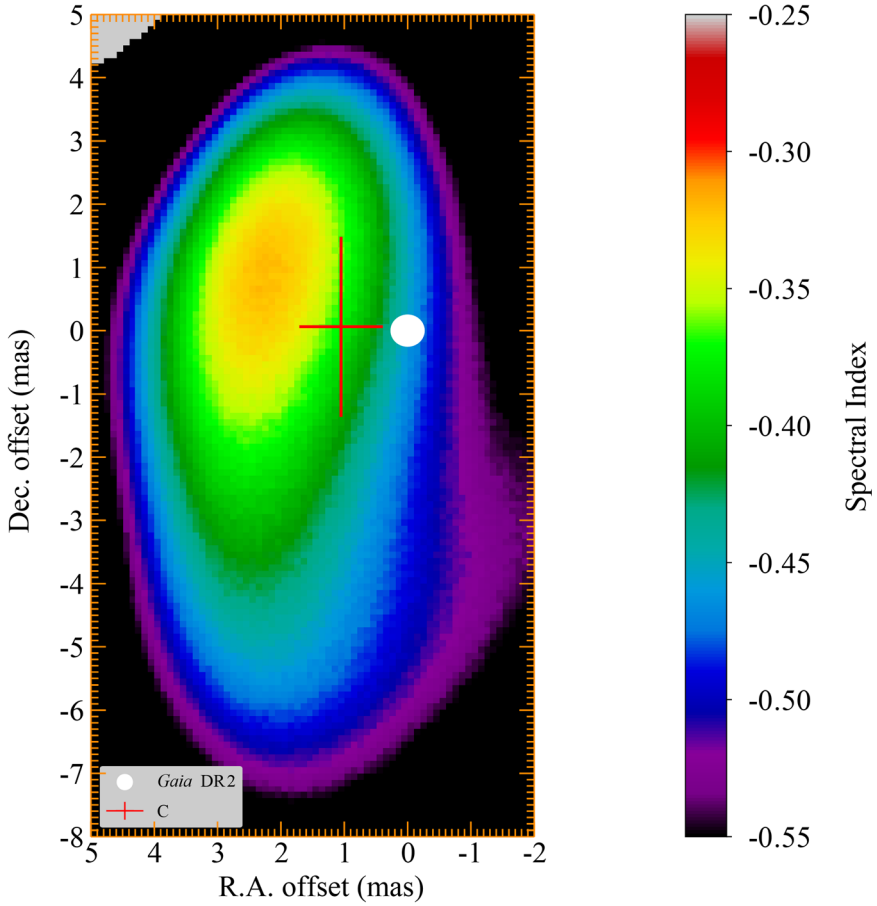

Figure 5. Comparison of positions between Gaia DR2 and VLBI component C in the spectral index map. Here, only the flat spectral region ($\alpha > -0.5$) is shown. We take a 3σ position error of component C here, where a 1σ position error is estimated through the method described in Section 2.3.

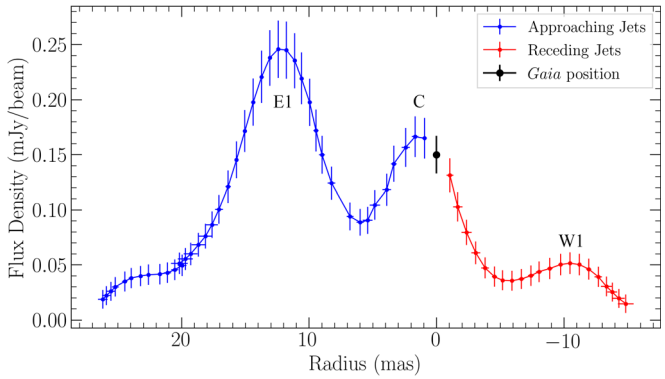

Figure 6. 5 GHz flux density distribution along the jet ridge line for I Zw 1. The data points with positive (blue) and negative (red) radii represent the approaching and receding jets, respectively. Positional uncertainties were directly measured in fitting the ridge line in Section 2.4 and flux uncertainties are estimated by accounting for thermal noise errors and calibration uncertainties (see Section 2.5).

super-Eddington rates, as observed in cases like SS 433 (Fabrika 2004) and V404 Cygni (Miller-Jones et al. 2019).

However, if the jet undergoes episodic eruptions, its significance lies in contributing to a unified framework for accreting systems at near/super-Eddington rates. This is significant because a canonical intermediate state commonly observed in XRBs is associated with near/super-Eddington rates and transient/episodic jets. There are many studies show that XRBs transitioning into a near/super-Eddington state are often accompanied by episodic jets (Revnivtsev et al. 2002; Done et al. 2004; Fabrika 2004; Miller-Jones et al. 2019). An intriguing example is the super-Eddington accreting XRB, V404 Cygni (Miller-Jones et al. 2019), which exhibits both precessing and transient ejection. In observations, there is also growing evidence to show that highly accreting AGNs tend to launch episodic jets (Yao et al. 2021; Yang et al. 2022a, 2022b, 2022c, 2023).

3.4. Physical Interpretations of the Complex Jets

By summing the radio flux density along the jet trajectory, i.e., only excluding the component S, the measured 5 GHz jet luminosity of I Zw 1 is $\log L_{5\mathrm{GHz}} = 38.547 \pm 0.003$ erg s^{-1}. Taking the X-ray luminosity of $\log L_{2-10\mathrm{keV}} = 43.65$ erg s^{-1} measured in 2020 (Wilkins et al. 2021), the radio to X-ray luminosity ratio of I Zw 1 is $L_\mathrm{R}/L_\mathrm{X} = 10^{-5.102}$, suggesting the nature of the jet is the corona ejection from the accretion disk (Yuan et al. 2009), i.e., $L_\mathrm{R}/L_\mathrm{X} \sim 10^{-5}$ (Panessa et al. 2019; Yang et al. 2020), and consistent with the interpretation of the X-ray behavior (Gallo et al. 2007; Wilkins et al. 2017). Models and observational evidence suggest that episodic jets in both AGN and microquasars are ejected from the accretion disk corona (see Shende et al. 2019, and references therein).

The bilateral morphology and the linear size of ∼45 pc (the tapered 5 GHz image in panel (c) of Figures 1 and 6) are reminiscent of I Zw 1 being a compact symmetric object (CSO;

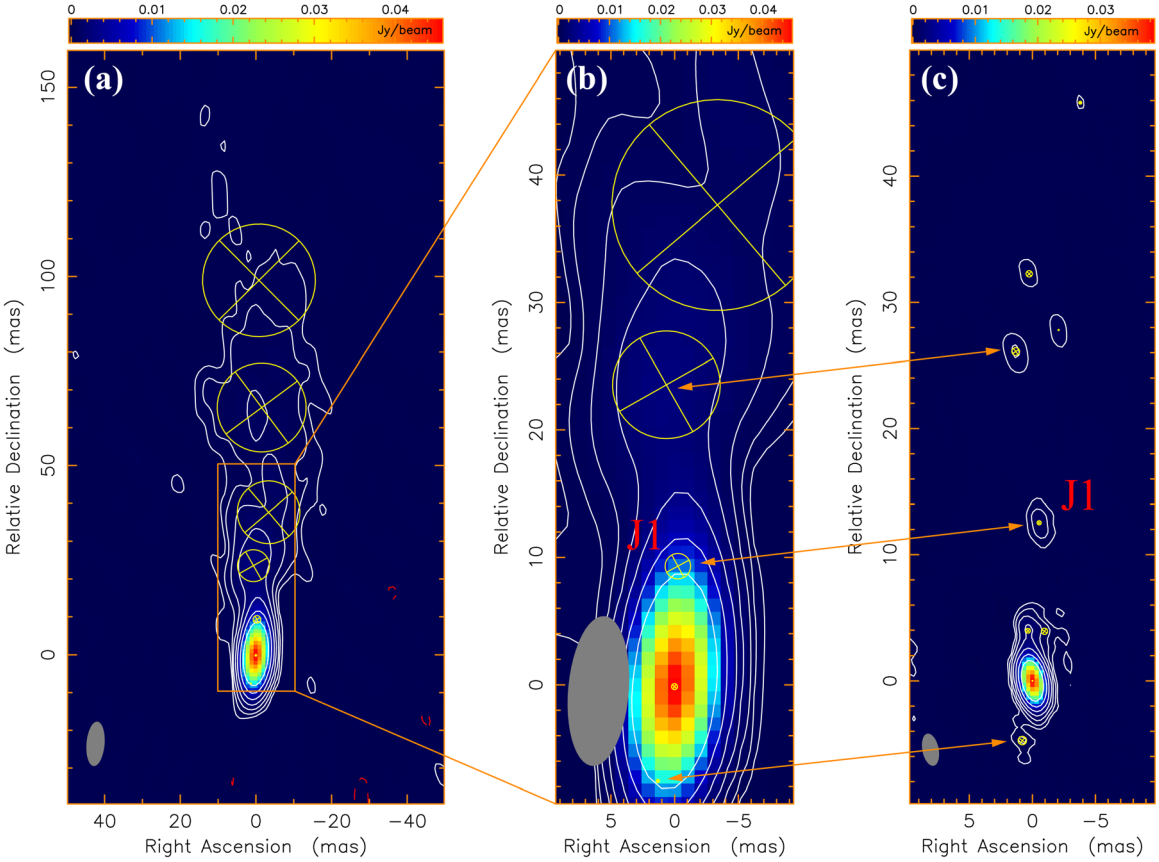

Figure 7. Model-fitting images of the phase calibrator J0056+1341 at 1.5 GHz (panel (a) and (b)) and 5 GHz (panel (c)). The images are produced using a two-dimensional Gaussian model fit with natural weights. The contours are plotted as $3\sigma \times (-1, 1, 2, 4, 8, ...)$, where σ is the rms noise. The white solid curves represent positive values, and the red-dashed curves represent negative values. The rms noise is 0.2 mJy beam^{-1} for both the 1.5 and 5 GHz images. The model-fitting components are superimposed as yellow circles. The gray ellipses in the bottom left corner of each panel represent the FWHM of the restoring beam. The gray lines between panels (c) and (b) indicate the corresponding components without the core shift effect, i.e., the optically thin components.

O'Dea & Saikia 2021). However, the lack of a spectral peak at the gigahertz range (Figure 3) alternatively implies that it belongs to compact steep-spectrum (CSS) radio sources. Assuming minimum energy (approximately equipartition) conditions in synchrotron emission, we can estimate the magnetic field $B_{\rm min}$ of I Zw 1 in units of Gauss through the formula (e.g., Miley 1980; Patil et al. 2022)

$$B_{\rm min} \approx 0.0152 \left[\frac{a}{f_{rl}} \frac{(1+z)^{4-\alpha}}{\theta^3} \frac{S_i}{\nu^\alpha} \frac{\nu_2^{p+\alpha} - \nu_1^{p+\alpha}}{r(p+\alpha)} \right]^{2/7} \text{(G)}, \quad (3)$$

where S_i (in millijansky) is the integrated flux density of the source measured at frequency ν (in gigahertz) and angular size θ (in mas), α is the spectral index, z is the redshift of the source, and r is the comoving distance in Mpc. Here, we take $p = 0.5$, the overall spectral index $\alpha = -0.89 \pm 0.10$ from $\nu_1 \sim 1$ GHz to $\nu_2 \sim 15$ GHz, a filling factor for the relativistic plasma $f_{rl} = 1$ and a relative contribution of the ions to the energy $a = 2$. By adopting the standard ΛCDM cosmology and using the cosmology calculator provided by NED,[23] $r = 245.7$ Mpc in this case. Here, we use the integrated flux density of 2.636 ± 0.282 mJy and the angular size of 50 mas from the tapered VLBA 1.5 GHz image, which yield an overall magnetic field of $B_{\rm min} \approx 10^{-3.6}$ G. The magnetic field is consistent with the typical value of, e.g., CSOs with peaked-spectrum (PS; $B \sim 10^{-3}$ G) and CSS ($B \sim 10^{-4}$ G) radio sources (O'Dea 1998). On the other hand, the total radio power of I Zw 1 is only $10^{21.8}$ W Hz^{-1} (from the 5 GHz EVN+*e*-MERLIN observational flux density of jets; see above), which is at least 1 order of magnitude lower than the typical samples of PS and CSS sources (O'Dea & Saikia 2021). However, the radio power of I Zw 1 remains higher than our recently discovered CSO/PS in NGC 4293 ($\sim 10^{20}$ W Hz^{-1}, see Yang et al. 2022c), which holds the current lower-limit record of radio power. Simultaneously, the magnetic field at component E1 can be estimated as $B_{\rm min} \approx 10^{-2.9}$ G by using the model-fitting results with either the 1.5 GHz VLBA or 5 GHz EVN+*e*-MERLIN observational result.

As the promising spectral turnover of I Zw 1 must be below 1 GHz, we can estimate the lowest allowed electron lifetime via the formula (O'Dea 1998)

$$t \simeq 8.22 \times \frac{B^{1/2}}{B^2 + B_R^2} \times ((1+z)\nu_p)^{-1/2} \text{ (yr)}, \quad (4)$$

where B is the magnetic field in gauss, $B_{\rm R} \simeq 4(1+z)^2 \times 10^{-6}$ G is the equivalent magnetic field of the microwave background, and ν_p is the break frequency in gigahertz. For I Zw 1, using the values estimated above, i.e., $B \approx 10^{-3.6}$ G and $\nu_p < 1$ GHz, we find the

[23] https://www.astro.ucla.edu/~wright/CosmoCalc.html

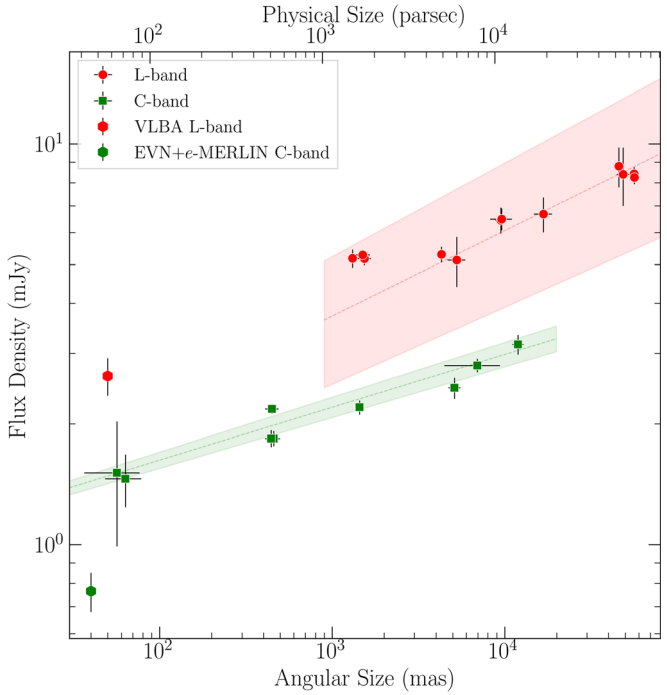

Figure 8. The radio flux density of I Zw 1 over characteristic sizes of emission regions ranging from ∼0.″04 to ∼50″. The integrated radio flux densities and uncertainties of I Zw 1 in the *L* and *C* bands are shown (Table 2). As I Zw 1 is not resolved in the given observations, the synthesized beams are taken to represent the characteristic sizes of emission regions. The dashed lines and belts show power-law fittings and 95% confidence intervals, respectively, in the *L* (red) and *C* bands (green).

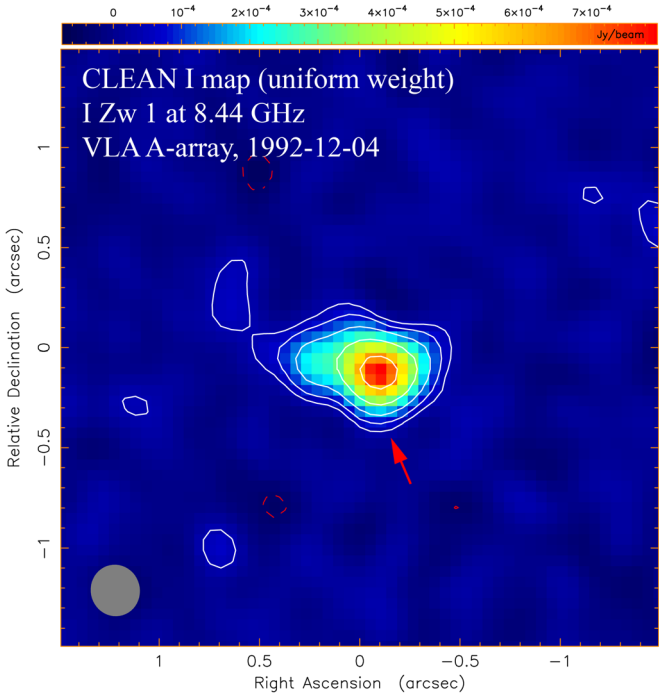

Figure 9. VLA A-array 8.4 GHz image of I Zw 1. Gaia DR2 position of I Zw 1 is set as the map center. The image peak is 0.798 mJy beam^{-1}. The contours are at $3\sigma \times (-1, 1, 2, 2, 4, 8, ...)$ and $1\sigma = 0.038$ mJy beam^{-1}, where positive contours are displayed in white, and negative ones are shown by red hash marks. The FWHM of the restoring beam is 0.″258 × 0.″245 at 12.°7 and displayed as gray ellipses in the lower-left corner. The red arrow marks a possible southern bump.

electron lifetime is substantially $>10^{6.3}$ yr. Again, the estimated electron lifetime of component E1 is $>10^{5.2}$ yr. Taking component E1 as a reference (15 mas away from the core) and assuming a typical knot advance speed of 0.1*c* for PS/CSS (O'Dea & Saikia 2021), the ejection timescale of component E1 is only ∼550 yr and smaller than its electron lifetime above; therefore, this suggests the knot advance speed of I Zw 1 should be substantially slower than 0.1 *c*. In stellar-mass XRBs, discrete radio blobs are produced in the very high state or super-Eddington state at a timescale spanning from a few days to 1 yr (to the best of our knowledge, see Margon & Anderson 1989; Mirabel & Rodríguez 1994; Hjellming & Rupen 1995; Fender et al. 1999; Tudose et al. 2007; Joseph et al. 2011; Miller-Jones et al. 2012, 2019; Bright et al. 2020). The longer ejection timescale in I Zw 1 seems to be more consistent with its more massive nucleus than XRBs, i.e., the ejection timescale can be scaled through the mass of accretors, which supports the scale-invariant ejection process in both XRBs and AGNs.

Component S in the VLBA 1.5 GHz image is a real structure (panel (b) of Figure 1), as it is identified in the 1.5 GHz tapered map (panel (a) of Figure 1). The 5 GHz EVN image fails to detect component S possibly due to the loss of large-scale and diffuse emission. The radio emission at component S is likely responsible for the flux density deficit at 5 GHz (see Figure 8). Furthermore, the southern bump in the VLA image (Figure 9) mimics component S, which requires further identification. Interestingly, component S clearly deviates from the jet trajectory because the jet is along the east–west direction and extends up to 0.″5 scale (see Figure 9). Here, we interpret the bending of component S as the result of jet–medium interactions. Given that the jet direction (extending up to ∼0.5 pc) is nearly aligned with the kiloparsec-scale molecular disk (Tan et al. 2019; Shangguan et al. 2020) in I Zw 1, it is possible to support a jet–disk interaction. On the other hand, I Zw 1 hosts strong multiscale wide-angle outflows: an ultrafast wind-like outflow with a velocity of $>0.25\,c$ obtained from the fitting of the iron K-line profile (Reeves & Braito 2019), an ionized ultraviolet gas outflow with a velocity of 1870 km s^{-1} (Laor et al. 1997) and X-ray outflow with velocities of ∼2000 km s^{-1} (Costantini et al. 2007; Silva et al. 2018), and a neutral gas outflow with a velocity of 45 km s^{-1} (Rupke et al. 2017). Given that the wide-angle outflows tend to be perpendicular to the kiloparsec-scale molecular disk, for example, the neutral gas outflow (see Rupke et al. 2017, for their Figure 13) of I Zw 1 is along the north–south direction; therefore, component S can be a result of jet-wind collision as well.

4. Summary

In summary, AGNs with near or super-Eddington accretion rates are often discussed as a scaled-up version of the stellar-mass black hole in the very high state or ultraluminous state. The observational evidence of episodic jets in I Zw 1 indicates that the analogy between AGNs and XRBs might also hold in this extreme state. Our observations imply that near or super-Eddington and extremely radio-quiet AGNs can also launch short-lived, small-scale, and weak jets. In Appendix B, we present further analysis of the radio emission in I Zw 1, which sheds light on the long-standing question about the origin of radio emission in radio-quiet AGNs. Such a population is important for building our understanding of jet–disk coupling in near or super-Eddington states. There is only one Galactic microquasar (SS 433) that exhibits a long timescale, super-

Eddington behavior, and quasicontinuous ejection (Fabrika 2004). Only a few XRBs evolve into a near/super-Eddington state and are associated with episodic jets (Revnivtsev et al. 2002; Done et al. 2004; Fabrika 2004; Miller-Jones et al. 2019), but this phase is short lived. Finally, the radio emission from a handful of (extragalactic) ULX sources is too weak to be detected (Kaaret et al. 2017). The timescale of the super-Eddington state in AGNs is longer than the canonical very high state in XRBs according to the scaling relation, and the radio luminosity of the super-Eddington state in AGNs is higher than that of SBHs, according to the relation $L_R/L_X = 10^{-5}$ (Panessa et al. 2019; Yang et al. 2020), which is essential for testing the generic model of jet–disk coupling for all near/super-Eddington systems. Our findings here may indicate common features for high-Eddington AGNs because there are similar knots/discrete radio blobs in jets and corresponding transverse/bending structures in other sources, e.g., NGC 4051 (Giroletti & Panessa 2009) with an Eddington ratio of 0.2 (Yuan et al. 2021) and Mrk 335 (Yao et al. 2021) with an Eddington ratio ranging from 0.48–3.11 (Yang et al. 2020). Further observational and theoretical studies will be necessary to establish a comprehensive understanding of the outflows of near/super-Eddington AGNs, and the results obtained from this work may contribute to this goal.

Acknowledgments

This work is supported by the National Science Foundation of China (12103076, 11721303, 11991052), the National Key R&D Program of China (2016YFA0400702, 2018YFA0404602, 2018YFA0404603). X.Y. acknowledges the support of the Shanghai Sailing Program (21YF1455300) and the China Postdoctoral Science Foundation (2021M693267). S.Y. was supported by an Alexander von Humboldt Foundation Fellowship. J.S. acknowledges financial support from the Czech Science Foundation project No.19-05599Y. M.F.G. is supported by the Shanghai Pilot Program for Basic Research Chinese Academy of Science, Shanghai Branch (JCYJ-SHFY-2021-013), the National SKA Program of China (grant No. 2022SKA0120102), and the science research grants from the China Manned Space Project No. CMSCSST-2021-A06. Scientific results from data presented in this publication are derived from the EVN project EY037 and the VLBA project BY145. EVN is a joint facility of independent European, African, Asian, and North American radio astronomy institutes. *e*-MERLIN is a National Facility operated by the University of Manchester at Jodrell Bank Observatory on behalf of STFC. The National Radio Astronomy Observatory is a facility of the National Science Foundation operated under cooperative agreement by Associated Universities, Inc. This work has made use of data from the European Space Agency (ESA) mission Gaia,[24] processed by the Gaia Data Processing and Analysis Consortium (DPAC).[25] Funding for the DPAC has been provided by national institutions, in particular, the institutions participating in the Gaia Multilateral Agreement.

Appendix A
Large-scale Radio Emission

Figure 3 shows I Zw 1 has a power-law radio spectrum over the entire observed frequency range. This indicates the dominance of synchrotron radiation, and it is not significantly affected by the characteristic size of emission regions (see Figure 8), where the intercept between the *L*- and *C*-band lines can be regarded as the spectral index. The overall spectral index is -0.89 ± 0.10, and there is no significant decrease at higher frequencies, indicating a continuous replenishment of fresh electrons (Morganti 2017). Interestingly, the spectral index at the jet edge farthest from the core is ~ -1.8 (Figure 4). This is inconsistent with the overall spectral index estimated for the larger area but suggests a non-jet origin because the spectral index decreases along the jet trajectory. The large-scale flux density is dominated by diffuse radio emission with only a fraction coming from the (parsec scale) core region (only account ∼30% and ∼47% of radio emission from 60 kpc and ∼1.54 kiloparsec-scale region at 1.5 GHz, respectively). The distribution of radio flux density can be fitted as $S_L = (0.85 \pm 0.18) r^{0.212 \pm 0.020}$ and $S_C = (0.88 \pm 0.02) r^{0.131 \pm 0.005}$, where S_L and S_C are the *L*- and *C*-band flux density in millijansky, and r is the characteristic size of emission regions in mas (see Figure 8). Specifically, the characteristic size of emission regions reflects spatial-filtering characteristics of the genuine emission structure, and this denotes the solution achieved under the observing baselines (UV coverage). The VLBA 1.5 GHz emission satisfies the flux density versus beam size distribution, while the 5 GHz flux density from our EVN+*e*-MERLIN observation is underestimated, due to the loss of large-scale emissions.

Both star-forming activities and relativistic winds can produce large-scale radio emission (Panessa et al. 2019). Here, the star-forming activities are preferentially referred to as supernovae or supernova remnants, due to the power-law spectrum. Assuming all of the radio emission is from star-forming activities, we can estimate the star formation rate (SFR) from radio emission by using the SFR–radio relation (formula 3 in Yang et al. 2020). The largest SFR can be obtained from the data sets: NVSS at 1.4 GHz, AE0022 at 1.4 GHz and 4.86 GHz, and AA0048 at 14.94 GHz. These yield an SFR of $\sim 20\, M_\odot\, \mathrm{yr}^{-1}$, which is similar to other estimates (Molina et al. 2021) of $\sim 26\, M_\odot\, \mathrm{yr}^{-1}$, suggesting the large-scale radio emission can be entirely due to star-forming activities, while the SFR–radio relation is crude, and we cannot fully rule out the contribution of wind-like outflow, the radio-emitting wind at large scales (a few kiloparsec scales) is negligible. In addition, the radio-emitting wind is still possible at the intermediate scale (tens of parsec scale), as there are no compact supernovae and supernova remnants detected in our VLBI and *e*-MERLIN observations (e.g., Fenech et al. 2008).

ORCID iDs

Xiaolong Yang https://orcid.org/0000-0002-4439-5580
Su Yao https://orcid.org/0000-0002-9728-1552
Luigi C. Gallo https://orcid.org/0000-0000-0000-0000
Jun Yang https://orcid.org/0000-0002-2322-5232
Luis C. Ho https://orcid.org/0000-0001-6947-5846
Minfeng Gu https://orcid.org/0000-0002-4455-6946
Willem A. Baan https://orcid.org/0000-0003-3389-6838
Jiri Svoboda https://orcid.org/0000-0003-2931-0742
Ran Wang https://orcid.org/0000-0003-4956-5742
Xiang Liu https://orcid.org/0000-0001-9815-2579
Xiaoyu Hong https://orcid.org/0000-0002-1992-5260
Xue-Bing Wu https://orcid.org/0000-0002-7350-6913
Wei Zhao https://orcid.org/0000-0003-4478-2887

[24] https://www.cosmos.esa.int/gaia
[25] https://www.cosmos.esa.int/web/gaia/dpac/consortium

References

Baczko, A. K., Schulz, R., Kadler, M., et al. 2019, A&A, 623, A27
Bardeen, J. M., & Petterson, J. A. 1975, ApJL, 195, L65
Barvainis, R., & Antonucci, R. 1989, ApJS, 70, 257
Barvainis, R., Lonsdale, C., & Antonucci, R. 1996, AJ, 111, 1431
Bian, W.-H., & Zhao, Y.-H. 2003, PASJ, 55, 599
Blandford, R. D., & Payne, D. G. 1982, MNRAS, 199, 883
Blandford, R. D., & Znajek, R. L. 1977, MNRAS, 179, 433
Bright, J. S., Fender, R. P., Motta, S. E., et al. 2020, NatAs, 4, 697
Condon, J. J., Cotton, W. D., Greisen, E. W., et al. 1998, AJ, 115, 1693
Condon, J. J., Huang, Z. P., Yin, Q. F., & Thuan, T. X. 1991, ApJ, 378, 65
Costantini, E., Gallo, L. C., Brandt, W. N., Fabian, A. C., & Boller, T. 2007, MNRAS, 378, 873
Dai, L., McKinney, J. C., Roth, N., Ramirez-Ruiz, E., & Miller, M. C. 2018, ApJL, 859, L20
Davis, S. W., & Laor, A. 2011, ApJ, 728, 98
Done, C., Gierliński, M., & Kubota, A. 2007, A&ARv, 15, 1
Done, C., Wardziński, G., & Gierliński, M. 2004, MNRAS, 349, 393
Dressel, L. L., & Condon, J. J. 1978, ApJS, 36, 53
Edelson, R. A. 1987, ApJ, 313, 651
Esin, A. A., McClintock, J. E., & Narayan, R. 1997, ApJ, 489, 865
Fabrika, S. 2004, Astrophys. Space Phys. Res., 12, 1
Falcke, H., Körding, E., & Markoff, S. 2004, A&A, 414, 895
Fender, R. P., Belloni, T. M., & Gallo, E. 2004, MNRAS, 355, 1105
Fender, R. P., Garrington, S. T., McKay, D. J., et al. 1999, MNRAS, 304, 865
Fendt, C., & Sheikhnezami, S. 2013, ApJ, 774, 12
Fenech, D. M., Muxlow, T. W. B., Beswick, R. J., Pedlar, A., & Argo, M. K. 2008, MNRAS, 391, 1384
Fomalont, E. B. 1999, in ASP Conf. Ser. 180, Synthesis Imaging in Radio Astronomy II, ed. G. B. Taylor, C. L. Carilli, & R. A. Perley (San Francisco, CA: ASP), 301
Fromm, C. M., Perucho, M., Porth, O., et al. 2018, A&A, 609, A80
Fromm, C. M., Ros, E., Perucho, M., et al. 2013, A&A, 557, A105
Gaia Collaboration, Katz, D., Antoja, T., et al. 2018a, A&A, 616, A11
Gaia Collaboration, Brown, A. G. A., Vallenari, A., et al. 2018b, A&A, 616, A1
Gallimore, J. F., Baum, S. A., & O'Dea, C. P. 1997, Natur, 388, 852
Gallo, L. C., Brandt, W. N., Costantini, E., & Fabian, A. C. 2007, MNRAS, 377, 1375
Giroletti, M., & Panessa, F. 2009, ApJL, 706, L260
Gladstone, J. C., Roberts, T. P., & Done, C. 2009, MNRAS, 397, 1836
Greiner, J., Cuby, J. G., & McCaughrean, M. J. 2001, Natur, 414, 522
Greisen, E. W. 2003, in Astrophysics and Space Science Library, AIPS, the VLA, and the VLBA, ed. A. Heck, Vol. 285 (Dordrecht: Kluwer), 109
Hjellming, R. M., & Rupen, M. P. 1995, Natur, 375, 464
Ho, L. C., & Kim, M. 2009, ApJS, 184, 398
Hovatta, T., Aller, M. F., Aller, H. D., et al. 2014, AJ, 147, 143
Huang, Y.-K., Hu, C., Zhao, Y.-L., et al. 2019, ApJ, 876, 102
Janssen, M., Falcke, H., Kadler, M., et al. 2021, NatAs, 5, 1017
Joseph, T. D., Maccarone, T. J., & Fender, R. P. 2011, MNRAS, 415, L59
Kaaret, P., Feng, H., & Roberts, T. P. 2017, ARA&A, 55, 303
Kadler, M., Ros, E., Lobanov, A. P., Falcke, H., & Zensus, J. A. 2004, A&A, 426, 481
Kameno, S., Inoue, M., Wajima, K., Sawada-Satoh, S., & Shen, Z.-Q. 2003, PASA, 20, 134
Kellermann, K. I., Sramek, R., Schmidt, M., Shaffer, D. B., & Green, R. 1989, AJ, 98, 1195
King, A., Lasota, J.-P., & Middleton, M. 2023, NewAR, 96, 101672
Körding, E. G., Jester, S., & Fender, R. 2006, MNRAS, 372, 1366
Kovalev, Y. Y., Lobanov, A. P., Pushkarev, A. B., & Zensus, J. A. 2008, A&A, 483, 759
Kovalev, Y. Y., Petrov, L., & Plavin, A. V. 2017, A&A, 598, L1
Kroupa, P., Subr, L., Jerabkova, T., & Wang, L. 2020, MNRAS, 498, 5652
Lacy, M., Baum, S. A., Chandler, C. J., et al. 2020, PASP, 132, 035001
Laor, A., Jannuzi, B. T., Green, R. F., & Boroson, T. A. 1997, ApJ, 489, 656
Lense, J., & Thirring, H. 1918, PhyZ, 19, 156
Lobanov, A. P. 2005, arXiv:astro-ph/0503225
Margon, B., & Anderson, S. F. 1989, ApJ, 347, 448
Marr, J. M., Taylor, G. B., & Crawford, F. I. 2001, ApJ, 550, 160
Martínez-Paredes, M., Aretxaga, I., Alonso-Herrero, A., et al. 2017, MNRAS, 468, 2
McMullin, J. P., Waters, B., Schiebel, D., Young, W., & Golap, K. 2007, in ASP Conf. Ser. 376, Astronomical Data Analysis Software and Systems XVI, ed. R. A. Shaw, F. Hill, & D. J. Bell (San Francisco, CA: ASP), 127
Middleton, M. J., Walton, D. J., Alston, W., et al. 2021, MNRAS, 506, 1045
Miley, G. 1980, ARA&A, 18, 165
Miller-Jones, J. C. A., Sivakoff, G. R., Altamirano, D., et al. 2012, MNRAS, 421, 468
Miller-Jones, J. C. A., Tetarenko, A. J., Sivakoff, G. R., et al. 2019, Natur, 569, 374
Mineshige, S., Kawaguchi, T., Takeuchi, M., & Hayashida, K. 2000, PASJ, 52, 499
Mirabel, I. F., & Rodríguez, L. F. 1994, Natur, 371, 46
Molina, J., Wang, R., Shangguan, J., et al. 2021, ApJ, 908, 231
Morganti, R. 2017, NatAs, 1, 596
Narayan, R., & Yi, I. 1994, ApJL, 428, L13
O'Dea, C. P. 1998, PASP, 110, 493
O'Dea, C. P., & Saikia, D. J. 2021, A&ARv, 29, 3
Panessa, F., Baldi, R. D., Laor, A., et al. 2019, NatAs, 3, 387
Patil, P., Whittle, M., Nyland, K., et al. 2022, ApJ, 934, 26
Perley, R. A., & Butler, B. J. 2017, ApJS, 230, 7
Petrov, L., & Kovalev, Y. Y. 2017, MNRAS, 467, L71
Plavin, A. V., Kovalev, Y. Y., & Petrov, L. Y. 2019, ApJ, 871, 143
Pogge, R. W. 2000, NewAR, 44, 381
Pradel, N., Charlot, P., & Lestrade, J. F. 2006, A&A, 452, 1099
Radcliffe, J. F., Garrett, M. A., Muxlow, T. W. B., et al. 2018, A&A, 619, A48
Reeves, J. N., & Braito, V. 2019, ApJ, 884, 80
Revnivtsev, M., Gilfanov, M., Churazov, E., & Sunyaev, R. 2002, A&A, 391, 1013
Rioja, M. J., Dodson, R., Orosz, G., Imai, H., & Frey, S. 2017, AJ, 153, 105
Rupke, D. S. N., Gültekin, K., & Veilleux, S. 2017, ApJ, 850, 40
Schinnerer, E., Eckart, A., & Tacconi, L. J. 1998, ApJ, 500, 147
Schmidt, M., & Green, R. F. 1983, ApJ, 269, 352
Shakura, N. I., & Sunyaev, R. A. 1973, A&A, 24, 337
Shangguan, J., Ho, L. C., Bauer, F. E., Wang, R., & Treister, E. 2020, ApJ, 899, 112
Shende, M. B., Subramanian, P., & Sachdeva, N. 2019, ApJ, 877, 130
Shepherd, M. C. 1997, in ASP Conf. Ser. 125, Astronomical Data Analysis Software and Systems VI, ed. G. Hunt & H. Payne (San Francisco, CA: ASP), 77
Silva, C. V., Costantini, E., Giustini, M., et al. 2018, MNRAS, 480, 2334
Sokolovsky, K. V., Kovalev, Y. Y., Pushkarev, A. B., & Lobanov, A. P. 2011, A&A, 532, A38
Svoboda, J., Guainazzi, M., & Merloni, A. 2017, A&A, 603, A127
Tan, Q.-H., Gao, Y., Kohno, K., et al. 2019, ApJ, 887, 24
Thompson, A. R., Moran, J. M., & Swenson, G. W. 1986, Interferometry and Synthesis in Radio Astronomy (New York: Wiley)
Tudose, V., Fender, R. P., Garrett, M. A., et al. 2007, MNRAS, 375, L11
Ulvestad, J. S., Antonucci, R. R. J., & Barvainis, R. 2005, ApJ, 621, 123
Urry, C. M., & Padovani, P. 1995, PASP, 107, 803
Vega-García, L., Lobanov, A. P., Perucho, M., et al. 2020, A&A, 641, A40
Vermeulen, R. C., Ros, E., Kellermann, K. I., et al. 2003, A&A, 401, 113
Vierdayanti, K., Sadowski, A., Mineshige, S., & Bursa, M. 2013, MNRAS, 436, 71
White, R. L., Becker, R. H., Helfand, D. J., & Gregg, M. D. 1997, ApJ, 475, 479
Wilkins, D. R., Gallo, L. C., Costantini, E., Brandt, W. N., & Blandford, R. D. 2021, Natur, 595, 657
Wilkins, D. R., Gallo, L. C., Silva, C. V., et al. 2017, MNRAS, 471, 4436
Yang, J., Paragi, Z., Frey, S., et al. 2023, MNRAS, 520, 5964
Yang, J., Yang, X., Wrobel, J. M., et al. 2022a, MNRAS, 514, 6215
Yang, X., Mohan, P., Yang, J., et al. 2022b, ApJ, 941, 43
Yang, X., Wang, R., & Guo, Q. 2022c, MNRAS, 517, 4959
Yang, X., Yao, S., Yang, J., et al. 2020, ApJ, 904, 200
Yao, S., Yang, X., Gu, M., et al. 2021, MNRAS, 508, 1305
Yuan, F., Lin, J., Wu, K., & Ho, L. C. 2009, MNRAS, 395, 2183
Yuan, F., & Narayan, R. 2014, ARA&A, 52, 529
Yuan, W., Macri, L. M., Peterson, B. M., et al. 2021, ApJ, 913, 3